Diamond nonlinear photonics

B. J. M. Hausmann[‡], I. Bulu[†‡], V. Venkataraman[‡], P. Deotare[†] and M. Lončar[*]

Despite progress towards integrated diamond photonics[1-4], studies of optical nonlinearities in diamond have been limited to Raman scattering in bulk samples[5]. Diamond nonlinear photonics, however, could enable efficient, *in situ* frequency conversion of single photons emitted by diamond's colour centres[6,7], as well as stable and high-power frequency microcombs[8] operating at new wavelengths. Both of these applications depend crucially on efficient four-wave mixing processes enabled by diamond's third-order nonlinearity. Here, we have realized a diamond nonlinear photonics platform by demonstrating optical parametric oscillation via four-wave mixing using single-crystal ultrahigh-quality-factor (1×10^6) diamond ring resonators operating at telecom wavelengths. Threshold powers as low as 20 mW are measured, and up to 20 new wavelengths are generated from a single-frequency pump laser. We also report the first measurement of the nonlinear refractive index due to the third-order nonlinearity in diamond at telecom wavelengths.

Diamond, as an attractive platform for on-chip photonics[1,9], combines the advantages of a high refractive index ($n = 2.4$) and low absorption losses within its large transmission window (from the ultraviolet to far-infrared). Diamond also offers excellent thermal properties (high thermal conductivity and low thermo-optic coefficient), enabling high power handling capabilities[10]. In addition, a relatively high nonlinear refractive index[11,12] ($n_2 = 1.3 \times 10^{-19}$ m^2 W^{-1} for visible wavelengths) and the lack of two-photon absorption (owing to its large bandgap of 5.5 eV) make diamond a promising candidate for integrated nonlinear optics over a wide wavelength range, spanning the visible and infrared. To date, on-chip nonlinear nanophotonic systems have been realized in various material platforms, including silica[13], silicon[14], Si$_3$N$_4$ (ref. 15) and III–V materials[16,17]. Some of these materials have even been used to implement microresonator-based high-repetition-rate frequency combs (up to terahertz)[8,15,18–20]. The diamond nonlinear photonics platform that we demonstrate here could potentially extend the operating range of microcombs to new wavelengths, resulting in temperature-stabilized frequency combs over a wide wavelength range. Moreover, diamond offers the unique opportunity to combine nonlinear photonics with quantum optics: for instance, diamond nonlinearities could allow for frequency translation (to the telecom wavelength range for example[7]) and pulse shaping[21,22] of single photons generated by its numerous colour centres, which often emit in the visible. These processes promise the coalescence of quantum information science with classical optical information-processing systems on the same chip.

As a consequence of an inversion symmetry in its crystal lattice, diamond's lowest-order non-zero nonlinear susceptibility[12] is $\chi^{(3)}$. A third-order nonlinear parametric process where two pump photons at frequency ν_P are converted to two different photons at ν_+ and ν_- (denoted signal and idler, respectively), such that energy conservation is satisfied by $2\nu_P = \nu_+ + \nu_-$, is called four-wave mixing (FWM). The FWM gain scales with the pump intensity, and the pump power requirement can be reduced by confining the light to nanowaveguides[23]. In addition to energy conservation, FWM in a waveguide also entails momentum conservation or phase-matching, which implies $\Delta k = 2\gamma P_p - \Delta k_L \approx 0$ (refs 23,24). Here, the second term $\Delta k_L = 2k_p - k_+ - k_-$ is the phase mismatch due to the linear dispersion (k_p, k_+ and k_- are the pump, signal and idler wavenumbers, respectively), $\gamma = 2\pi\nu_p n_2/cA_{eff}$ is the effective nonlinearity and A_{eff} the effective optical mode area. The term $2\gamma P_p$ arises from the nonlinear response to the strong pump, which imposes self-phase modulation (SPM) on itself and cross-phase modulation (XPM) on the generated modes that is twice as large as the SPM[18,25]. This nonlinear phase shift needs to be compensated for by the linear dispersion, that is, $\Delta k_L > 0$. Consequently, the group velocity dispersion (GVD) of the optical mode needs to be anomalous around the pump wavelength[23,24]; that is, GVD $= -(\lambda/c) \cdot d^2 n_{eff}/d\lambda^2 > 0$, where n_{eff} is the effective index of the waveguide, λ is the wavelength and c is the speed of light in vacuum.

The FWM efficiency can be drastically increased by using high-Q resonators[14,26], where photons make multiple round-trips on resonance, resulting in the optical intensity being enhanced by a factor of the finesse. Optical parametric oscillation (OPO) is achieved when the round-trip FWM gain exceeds the loss in the resonator, a process analogous to a laser above threshold, and bright coherent light is generated at the signal and idler wavelengths. In our diamond ring resonators (Fig. 1), momentum is intrinsically conserved because the optical modes are angular momentum eigenstates[27]. In this case, anomalous dispersion is required to achieve energy conservation between the cavity modes m (with different angular momentum) that participate in the FWM process[18]. This implies that the frequency separation between adjacent modes of the ring resonator, $|\nu_m - \nu_{m-1}|$ (or the free-spectral range, FSR), increases as a function of the mode number m. The resonator dispersion D_2, given by the change in the FSR ($\nu_{m+1} + \nu_{m-1} - 2\nu_m$), thus needs to be positive for modes around the pump wavelength[18,28]. The unequal frequency spacing of the resonator modes due to anomalous dispersion is compensated by nonlinear optical mode pulling, that is, a shift in the resonance frequencies caused by SPM and XPM due to the pump[18,25].

The intrinsic material dispersion of diamond is normal at telecom wavelengths. The net waveguide dispersion can be engineered to be anomalous through geometrical dispersion by appropriately designing the cross-sectional dimensions[15,20,23,28]. However, our fabrication technique (see Methods) relies on thin single-crystal diamond (SCD) films, which are typically wedged, resulting in a thickness variation of at least 300 nm across a millimeter-sized sample[9]. This effect occurs as a result of the mechanical polishing process for thin diamond plates (~20 μm thick) that are used to realize our diamond-on-insulator platform[4]. Accordingly, the ring resonator design has to be robust and the dispersion insensitive to
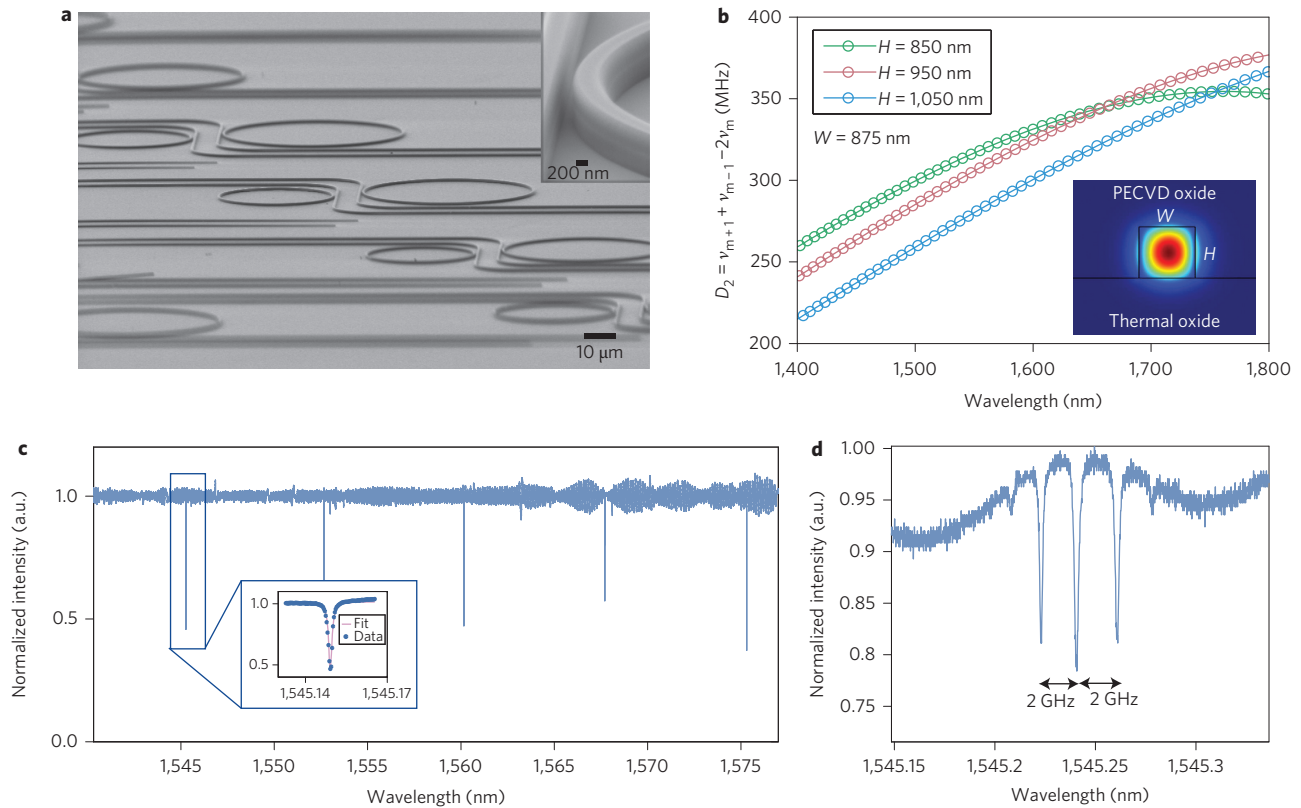
Figure 1 | Integrated ultrahigh-Q SCD ring resonators. a, Scanning electron microscope (SEM) image of an array of waveguide-coupled SCD ring resonators on a SiO$_2$/Si substrate. Before testing, chips were covered with 3 μm of PECVD-deposited silica. Inset: magnified view of the ring waveguide-coupling section with a ~475 nm gap size for the measured device. The rings are ~850 nm high, ~875 nm wide and have radii of 20–30 μm. **b**, Robust dispersion engineering allows for a range of ring heights to yield anomalous dispersion in the wavelength range of interest for a ring width of 875 nm. Inset: ring resonator optical mode profile in the diamond waveguide surrounded by silica. **c**, Normalized transmission spectrum of a ring resonator reveals high Q-factor modes. The radius of the ring is 20 μm, corresponding to an FSR of ~7.5 nm (~925 GHz). Inset: a loaded Q-factor of $Q_L \approx 1 \times 10^6$ is inferred from a Lorentzian fit for the mode at 1,545.1 nm. **d**, Light from our tunable laser is phase-modulated at 2 GHz to produce side bands that are then used as a ruler to calibrate the wavelength axis in our transmission measurements. Using this approach, loaded Q-factors as high as $Q_L \approx 1.14 \times 10^6$ are estimated.

variations in the diamond film thickness. The inset of Fig. 1b presents the mode profile for our geometry, a diamond ring resonator on top of a SiO$_2$/Si substrate and capped with a deposited SiO$_2$ layer. Figure 1b shows that, for a ring width of 875 nm, the resonator dispersion can be made anomalous in the wavelength range of interest for a range of film thicknesses (ring heights, H). Furthermore, for a ring resonator of radius 20 μm, anomalous dispersion for the transverse-electric (TE) mode can be achieved in the 1,300–1,800 nm wavelength range for widths of 800–900 nm and heights of 500–1,000 nm. This is well within our fabrication tolerances; Fig. 1a shows waveguide-coupled SCD ring resonators with radii of 20 and 30 μm, fabricated according to a method we have recently presented[9] (see Methods).

To characterize the diamond resonators we used a fibre-coupled transmission set-up that has been described elsewhere[9,29]. First, transmission measurements were performed by sweeping a continuous-wave laser (Santec TSL-510) across the telecom wavelength range to measure the resonator quality factors Q and the coupling of the bus-waveguide to the rings (Fig. 1c). Most devices were found to be slightly under-coupled. Loaded Q-factors, Q_L, as high as 1×10^6 were measured for the TE mode, with most devices having $Q_L > 2 \times 10^5$. To ensure an accurate resonance linewidth measurement, a radiofrequency phase modulation was imparted on the input light, which generated side bands around the main resonance (Fig. 1d). Comparing the linewidth of the resonance with the separation between the side bands (1–3 GHz) allowed for

a precise calibration of the wavelength/frequency axis[30]. Using this method, we measured a record-high $Q_L \approx 1.14 \times 10^6$ and inferred an intrinsic Q-factor of $Q_{int} \approx 1.35 \times 10^6$ and a waveguide propagation loss of 0.34 dB cm^{-1}.

The high pump powers required for OPO were obtained by sending the input laser through an erbium-doped fibre amplifier (Manlight). The pump was initially slightly blue-detuned and then slowly moved into resonance. The power absorbed by the ring caused a thermal redshift of the resonance, potentially arising due to heating of the silica cladding or surface effects at the diamond–silica interface. While tuning the laser deeper into resonance, the output light was monitored on an optical spectrum analyser (HP 70952B, Hewlett Packard). As the offset of the pump to the resonance minimum decreased, more power was transferred to the ring resonator, eventually resulting in the generation of pairs of new lines—at integer multiples of the resonator FSR—around the pump. The first side bands were generated at mode numbers $m \approx \sqrt{\kappa/D_2 \cdot \left(\sqrt{P_{in}/P_{th}} - 1 + 1\right)}$ away from the pump[28], where κ represents the resonator linewidth (cavity decay rate), D_2 is the resonator dispersion already discussed, P_{in} is the input pump power and P_{th} is the threshold pump power for parametric oscillation. Tuning the pump deeper into resonance generated several new modes further away from the pump, finally resulting in a spectrum of multiple lines with a frequency spacing given by the FSR (Fig. 2). The pump power coupled into the resonator is intrinsically stabilized
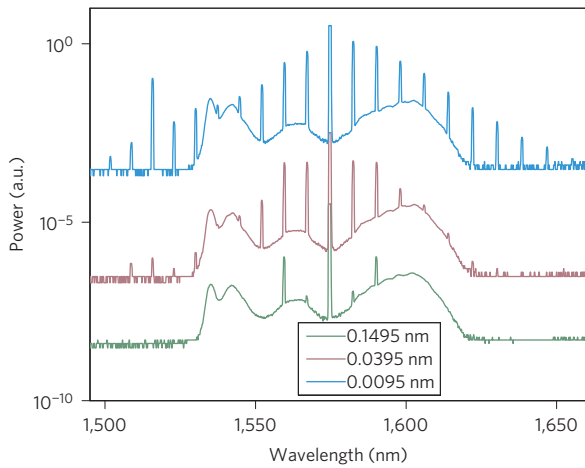
Figure 2 | OPO spectrum as a function of blue-detuning from resonance.
New frequencies are generated in the spectrum as the pump wavelength
approaches the resonance (transmission minimum) starting from a
blue-detuned position. The spectra are logarithmically offset for clarity.

during this entire process, achieving a thermal 'soft-lock'[31], and
stable oscillation was observed for up to ~20 min (limited by the
fibre-stage drifts).

The performance of our diamond OPO device was studied as a
function of pump wavelength. The same ring was pumped at two
different resonances, first at ~1,552 nm (C-band) and then at
~1,598 nm (L-band), and their output spectra were compared
(Fig. 3). For the same pump power of ~80 mW in the waveguide,
the former generates ten new lines spanning a range of 75 nm
while the latter generates 20 lines, spanning a range of 165 nm.
This effect can be explained by an increased power drop into the
ring for the larger ring-bus waveguide-coupling efficiency that
exists at longer wavelengths in our case (because the rings are
under-coupled). Additionally, this effect might be associated with
the change in dispersion with wavelength.

To determine the threshold for parametric oscillation, the output
power in the first generated side band was measured as a function of
pump power. Figure 4a shows the data for a device pumped at a res-
onance near 1,575 nm with $Q_L = 9.7 \times 10^5$, where we infer a P_{th} of

only ~20 mW in the waveguide and a conversion slope efficiency of
~2%. For pump powers above threshold, oscillation occurs into
multiple new modes, limiting the power converted to the first side
band. When pumping near 1,600 nm we infer the total power in
20 generated modes combined to be 3.9 mW (as estimated in the
waveguide) for an input pump power of 78 mW (in the waveguide)
and hence an overall conversion efficiency of ~5%.

The threshold power P_{th} for parametric oscillation arising from
the third-order nonlinearity (FWM) can also be estimated from
theory as[25,32]

$$P_{th} \approx 1.54\left(\frac{\pi}{2}\right)\frac{Q_C}{2Q_L} \cdot \frac{n^2\, V}{n_2 \lambda_P Q_L^2} \qquad (1)$$

where λ_P is the pump wavelength, V is the resonator mode volume
and n is the linear refractive index denoted earlier. Q_C and Q_L are the
coupling and loaded quality factors of the resonator, respectively. By
measuring P_{th} for various devices with different Q-factors, the non-
linear refractive index n_2 can be inferred in the wavelength range
around the pump. The measured P_{th} (estimated in the waveguide)
for eight different devices on the same chip is depicted in Fig. 4b.
From these data, we extract the first measurement of the nonlinear
refractive index of diamond in the telecom range as $n_2 = (8.2 \pm
3.5) \times 10^{-20}$ m^2 W^{-1}, which is a factor of 1.5 smaller than the n_2
value reported for visible wavelengths[11,12]. This is in good agreement
with the theoretical prediction of the dispersion of the nonlinear
susceptibility (longer wavelengths being more off-resonant from
the bandgap)[11]. Figure 4b also shows that most of the devices
measured are on the under-coupled side, consistent with the expec-
tations from transmission measurements.

We explored the limits of diamond nonlinear photonics using
numerical modelling and found that our ring resonators exhibit
anomalous dispersion (GVD > 0) over a wide bandwidth, spanning
850–2,350 nm, as shown in Fig. 5a. Thus, we believe that OPO gen-
eration beyond the current bandwidth of 165 nm in our devices is
only limited by the optical pump power propagating inside the reso-
nator and the resonator's optical losses. Larger pump powers,
enhanced by more efficient light in-coupling and larger Q-factors,
should enable the generation of octave-spanning, high-repetition-
rate, optical frequency combs that are of interest for numerous
applications[8,18,20,28,33,34]. Furthermore, diamond's large refractive
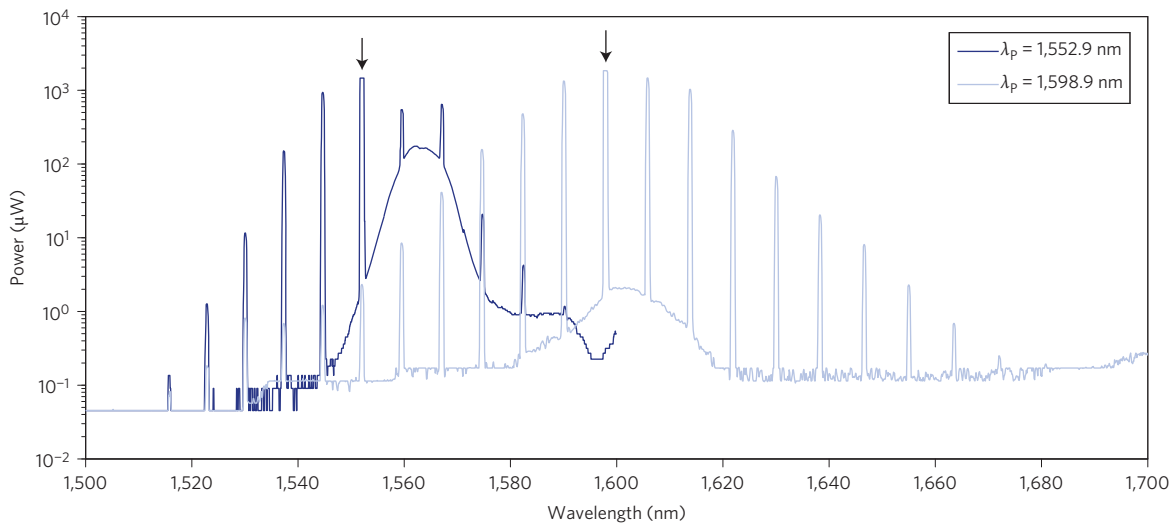

Figure 3 | OPO spectra for different pump wavelengths. The spectra, generated from the same ring resonator for two different pump wavelengths,
~1,553 nm and ~1,599 nm are shown. The pump power is the same in each case (~80 mW in the waveguide). A total of 20 new lines are generated when
pumping at ~1,599 nm, as opposed to ten lines when pumping at ~1,553 nm. This can be explained by the higher coupling efficiency between the
bus-waveguide and the ring resonator as well as a more favourable dispersion for longer wavelengths.
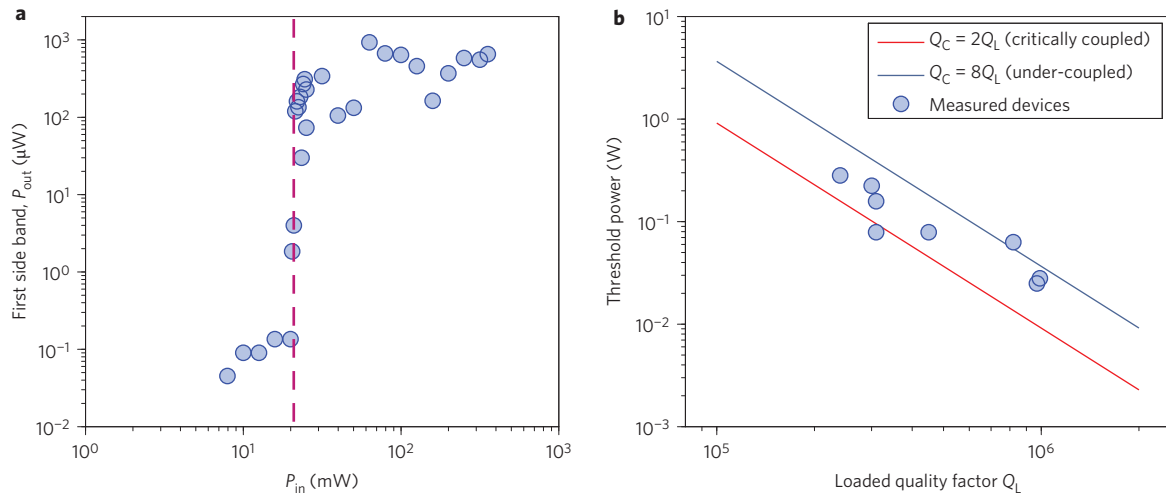
Figure 4 | Parametric oscillation threshold and its dependence on Q-factor. a, Output power in the first generated side band as a function of input pump power (both estimated in the waveguide) for a device with $Q_L = 9.7 \times 10^5$. The threshold for oscillation is observed to be 20 mW. **b**, Threshold powers for oscillation as a function of loaded quality factor Q_L (power estimated in the waveguide). Data are measured for eight different devices (blue dots). Threshold powers roughly follow the theoretically predicted trend of being inversely proportional to Q_L^2, with most devices being slightly under-coupled, that is, $Q_C > 2Q_L$ (consistent with the transmission measurements). The red line denotes critical coupling (100% transmission dip on-resonance), and the blue line denotes under-coupled resonators (50% transmission dip on-resonance).
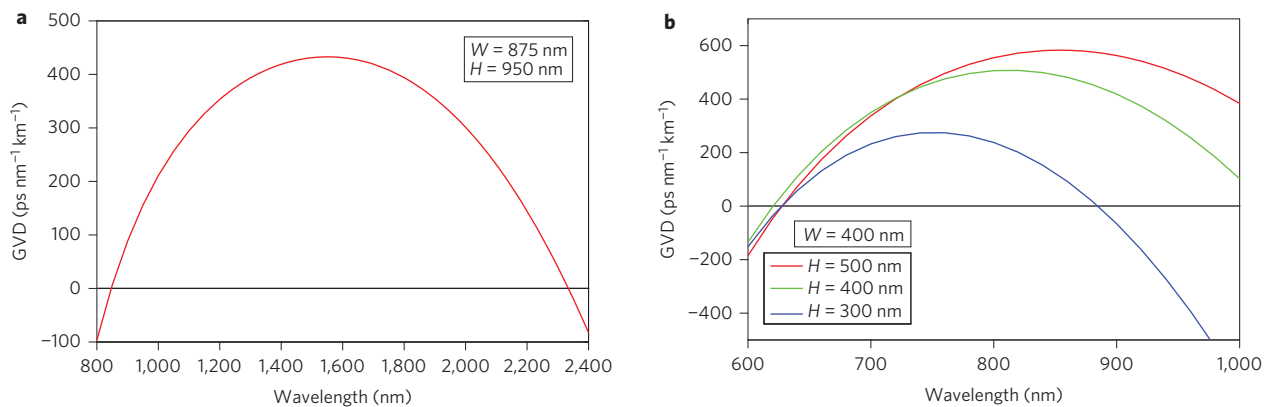

Figure 5 | Broadband anomalous dispersion of diamond waveguides embedded in silica. a, Devices designed for the telecom wavelength range (cross-section of 875 nm × 950 nm) show octave-spanning anomalous dispersion suitable for frequency comb generation. **b**, Smaller-cross-section waveguides (400 nm × 500 nm, 400 nm × 400 nm and 400 nm × 300 nm) allow for broadband anomalous dispersion, even in the visible wavelength range.

index allows for waveguides with anomalous dispersion even at visible wavelengths. For instance, a diamond waveguide with a 400 nm × 400 nm cross-section has GVD > 0 for a wavelength range of 620–1,020 nm, as shown in Fig. 5b. This feature has not been reported for other integrated nonlinear photonic platforms and, to the best of our knowledge, is a unique characteristic of the diamond nanophotonic platform presented in this work. Importantly, because of its wide bandgap, two-photon absorption and free-carrier absorption loss mechanisms are absent in diamond for wavelengths >440 nm. All of these characteristics of diamond, combined with its extremely large thermal conductivity and small thermo-optic coefficient, make diamond an excellent candidate for temperature-insensitive on-chip frequency combs, operating over the widest wavelength range, and capable of handling large optical powers.

In summary, we have demonstrated the first implementation of diamond nonlinear photonics on-chip, as exemplified in an OPO operating at telecom wavelengths, based on a fully integrated,

monolithic, SCD microresonator. The OPO leverages the $\chi^{(3)}$-nonlinearity of diamond to realize a FWM gain for sidebands around the pump frequency and is used to perform the first experimental measurement of $n_2 = (8.2 \pm 3.5) \times 10^{-20}$ m^2 W^{-1} for diamond in the telecom wavelength range. Ring resonators with ultrahigh Q-factors near 10^6 enable oscillation threshold powers as low as 20 mW in the bus-waveguide, and 20 sidebands spanning a wavelength range of 165 nm are generated with pump powers less than 100 mW. The total power generated in all sidebands was up to 5% of the pump power. These threshold levels and conversion efficiencies are comparable to those achieved in other more established material systems[15]. Despite the non-standard fabrication approach and wedging in our diamond films, we were able to achieve a reasonably high device yield of ~30%: out of 26 devices fabricated in a diamond film with dimensions of 570 μm × 630 μm, eight devices showed OPO action.

Another intriguing application of our nonlinear diamond photonic platform is the realization of continuous-wave, low-threshold,

on-chip Raman lasers emitting at exotic wavelengths[5]. This approach leverages diamond's giant Raman shift of 40 THz (due to its large optical phonon energy of 165 meV) and a large Raman gain of 15–75 cm GW^{-1}. Diamond is also host to a wide variety of colour centres capable of single-photon emission and is a promising material for quantum photonic networks[3,4]. Single-photon frequency conversion and pulse shaping, using diamond's nonlinearity, could potentially enable integrated quantum repeaters as well as long-distance quantum communication (when extended to the telecom wavelength range)[35]. Indeed, preliminary theoretical analysis of such quantum frequency conversion based on non-degenerate FWM shows promising efficiencies. For instance, we have estimated a single-photon conversion efficiency of 40% of the zero phonon line (ZPL) photons at 637 nm emitted by a nitrogen vacancy (NV) centre to 1.55 μm with modest pump powers of 50 mW, when using a geometry and Q-factors similar to those reported here (see Methods)[6,7]. Our work thus opens up an avenue for research in diamond nonlinear photonics, where all-optical information-processing on-chip may be realized at both the classical and quantum levels.

Methods

Device fabrication. The fabrication process was based on the recently described approach for integrated SCD devices[9]. A 20- to 30-μm-thick type-Ib high-pressure high-temperature (HPHT) SCD slab (Element Six) was cleaned in boiling acids (nitric, sulphuric and perchloric, in equal ratios), then thinned to the desired device layer thickness by cycling through Ar/Cl$_2$, oxygen etch and Ar cooling steps in an inductively coupled plasma reactive ion etch chamber[36–38]. The diamond film was cleaned and etched on both sides to remove the layers affected by stress/strain from the polishing process. After a final acid clean, the sample was transferred to a SiO$_2$/Si substrate (2-μm-thick thermal SiO$_2$ layer). An etch mask was formed by electron-beam lithography (EBL, Elionix ELS-F125) using XR-1541-6 and Fox 16 electron-beam resist (spin-on-glass, Dow Corning). Previously, our EBL writing introduced periodic scattering centres along the circumference of the devices that led to split resonances of degenerate clockwise- and anticlockwise-propagating whispering gallery modes[9]. Here, we improved the EBL writing by careful design of the layout file in terms of continuous writing of the pattern, eliminating discontinuous jumps of the electron beam and division of the pattern into small segments, which potentially leads to the absence of split resonances and the observed ultrahigh Q-factors. The pattern was then transferred to the diamond film in a second oxygen plasma etch step. Polymer in- and out-coupling pads consisting of SU-8 resist with a 3 μm × 3 μm cross-section were then aligned with respect to the adiabatically tapered diamond waveguides in a second EBL step to extend the diamond waveguides to the ends of the substrate[29]. Finally, 3 μm of silica was deposited using plasma-enhanced chemical vapour deposition (PECVD), to cap the devices and to allow for controlled cleaving and polishing of the end facets.

Modelling. A finite-element mode solver (COMSOL) was used to simulate the diamond ring resonator dispersion. The material dispersion of both the thermally grown SiO$_2$ under the diamond devices and the capping SiO$_2$ deposited via PECVD was evaluated using ellipsometry measurements, and these data were included in mode calculations. To optimize coupling into the ring resonator modes, the gap between the coupling waveguide and the ring resonator was designed by three-dimensional finite-difference time-domain simulations (Lumerical). For the above-mentioned cross-sectional dimensions, gaps of 400–500 nm yielded coupling Q-factors $Q_C > 5 \times 10^5$.

Single-photon conversion estimation. We estimated a conversion efficiency of 40% from the NV ZPL at 637 nm to the telecom wavelength (1,550 nm) with 50 mW pump power. In this estimation we used similar resonator parameters as reported above, that is, a ring radius of 20 μm, a cross-sectional mode area of 0.5 μm^2 and intrinsic and coupling Q-factors, $Q_{int} = 1 \times 10^6$ and $Q_C = 1 \times 10^5$, respectively (over-coupled resonators), which correspond to a cavity–NV cooperativity of $C \approx 12$. These calculations were performed for a noiseless quantum frequency conversion scheme based on non-degenerate FWM, where two waves act as strong pumps and convert a signal photon into an idler photon, assuming that all four waves are on resonance with different modes of the cavity. The analysis is similar to that recently presented by Huang and colleagues[7]. Our estimate also assumes that the NV centre is near the centre of the waveguide forming the ring resonator, that is, close to the field maximum and ideally aligned in polarization. Given the fairly large size of our ring resonator and the density of NV centres that can be formed by nitrogen ion implantation, we expect to achieve NV centres positioned in the field maximum with fairly high probability. The conversion efficiency can be further improved by using smaller ring resonators or even photonic-crystal nanobeam resonators.

References

1. Aharonovich, I., Greentree, A. D. & Prawer, S. Diamond photonics. *Nature Photon.* **5**, 397–405 (2011).
2. Zaitsev, A. M. *Optical Properties of Diamond: A Data Handbook* (Springer-Verlag, 2001).
3. Faraon, A., Barclay, P. E., Santori, C., Fu, K.-M. C. & Beausoleil, R. G. Resonant enhancement of the zero-phonon emission from a colour centre in a diamond cavity. *Nature Photon.* **5**, 301–305 (2011).
4. Hausmann, B. J. M. *et al.* Integrated diamond networks for quantum nanophotonics. *Nano Lett.* **12**, 1578–1582 (2012).
5. Mildren, R. P., Butler, J. E. & Rabeau, J. R. CVD-diamond external cavity Raman laser at 573 nm. *Opt. Express* **16**, 18950–18955 (2008).
6. McCutcheon, M. W., Chang, D. E., Zhang, Y., Lukin, M. D. & Lončar, M. Broad-band spectral control of single photon sources using a nonlinear photonic crystal cavity. *Opt. Express* **17**, 22689–22703 (2009).
7. Huang, Y.-P., Velev, V. & Kumar, P. Quantum frequency conversion in nonlinear microcavities. *Opt. Lett.* **38**, 2119–2121 (2013).
8. Kippenberg, T. J., Holzwarth, R. & Diddams, S. A. Microresonator-based optical frequency combs. *Science* **332**, 555–559 (2011).
9. Hausmann, B. J. M. *et al.* Integrated high-quality factor optical resonators in diamond. *Nano Lett.* **13**, 1898–1902 (2013).
10. Nebel, C. & Ristein, J. *Semiconductors and Semimetals: Thin-Film Diamond I* (Elsevier Academic, 2004).
11. Levenson, M. D. & Bloembergen, N. Dispersion of the nonlinear optical susceptibility tensor in centrosymmetric media. *Phys. Rev. B* **10**, 4447–4464 (1974).
12. Boyd, R. W. *Nonlinear Optics* (Academic, 2008).
13. Ferrera, M. *et al.* Low-power continuous-wave nonlinear optics in doped silica glass integrated waveguide structures. *Nature Photon.* **2**, 737–740 (2008).
14. Turner, A. C., Foster, M. A., Gaeta, A. L. & Lipson, M. Ultra-low power parametric frequency conversion in a silicon microring resonator. *Opt. Express* **16**, 4881–4887 (2008).
15. Levy, J. S. *et al.* CMOS-compatible multiple-wavelength oscillator for on-chip optical interconnects. *Nature Photon.* **4**, 37–40 (2010).
16. Hartl, I., Imeshev, G., Fermann, M. E., Langrock, C. & Fejer, M. M. Integrated self-referenced frequency-comb laser based on a combination of fiber and waveguide technology. *Opt. Express* **13**, 6490–6496 (2005).
17. Jung, H., Xiong, C., Fong, K. Y., Zhang, X. & Tang, H. X. Optical frequency comb generation from aluminum nitride microring resonator. *Opt. Lett.* **38**, 2810–2813 (2013).
18. Del'Haye, P. *et al.* Optical frequency comb generation from a monolithic microresonator. *Nature* **450**, 1214–1217 (2007).
19. Razzari, L. *et al.* CMOS-compatible integrated optical hyper-parametric oscillator. *Nature Photon.* **4**, 41–45 (2010).
20. Okawachi, Y. *et al.* Octave-spanning frequency comb generation in a silicon nitride chip. *Opt. Lett.* **36**, 3398–3400 (2011).
21. Lavoie, J., Donohue, J. M., Wright, L. G., Fedrizzi, A. & Resch, K. J. Spectral compression of single photons. *Nature Photon.* **7**, 363–366 (2013).
22. Raymer, M. G. & Srinivasan, K. A. Manipulating the color and shape of single photons. *Phys. Today* **65**, 32–37 (2012).
23. Foster, M. A. *et al.* Broad-band optical parametric gain on a silicon photonic chip. *Nature* **441**, 960–963 (2006).
24. Hansryd, J., Andrekson, A., Westlund, M., Li, J. & Hedekvist, P. Fiber-based optical parametric amplifiers and their applications. *IEEE J. Sel. Top. Quantum Electron.* **8**, 506–520 (2002).
25. Kippenberg, T. J., Spillane, S. M. & Vahala, K. J. Kerr-nonlinearity optical parametric oscillation in an ultrahigh-Q toroid microcavity. *Phys. Rev. Lett.* **93**, 083904 (2004).
26. Absil, P. P. *et al.* Wavelength conversion in GaAs micro-ring resonators. *Opt. Lett.* **25**, 554–556 (2000).
27. Vahala, K. J. Optical microcavities. *Nature* **424**, 839–846 (2003).
28. Herr, T. *et al.* Universal formation dynamics and noise of Kerr-frequency combs in microresonators. *Nature Photon.* **6**, 480–487 (2012).
29. Deotare, P. B. *et al.* All optical reconfiguration of optomechanical filters. *Nature Commun.* **3**, 846 (2012).
30. Collot, L., Lefevre-Seguin, V., Brune, M., Raimond, J. M. & Haroche, S. Very high-Q whispering-gallery mode resonances observed on fused silica microspheres. *Europhys. Lett.* **23**, 327–334 (1993).
31. Del'Haye, P., Arcizet, O., Schliesser, A., Holzwarth, R. & Kippenberg, T. J. Full stabilization of a microresonator-based optical frequency comb. *Phys. Rev. Lett.* **101**, 053903 (2008).
32. Matsko, A. B., Savchenkov, A. A., Strekalov, D., Ilchenko, V. S. & Maleki, L. Optical hyperparametric oscillations in a whispering-gallery-mode resonator: threshold and phase diffusion. *Phys. Rev. A* **71**, 033904 (2005).
33. Foster, M. A. *et al.* Silicon-based monolithic optical frequency comb source. *Opt. Express* **19**, 14233–14239 (2011).

34. Savchenkov, A. A. *et al.* Kerr combs with selectable central frequency. *Nature Photon.* **5,** 293–296 (2011).
35. Marcikic, I., de Riedmatten, H., Tittel, W., Zbinden, H. & Gisin, N. Long-distance teleportation of qubits at telecommunication wavelengths. *Nature* **421,** 509–513 (2003).
36. Lee, C. L., Gu, E., Dawson, M. D., Friel, I. & Scarsbrook, G. A. Etching and micro-optics fabrication in diamond using chlorine-based inductively-coupled plasma. *Diam. Relat. Mater.* **17,** 1292–1296 (2008).
37. Hausmann, B. J. M. *et al.* Fabrication of diamond nanowires for quantum information processing applications. *Diam. Relat. Mater.* **19,** 621–629 (2010).
38. Maletinsky, P. *et al.* A robust scanning quantum sensor for nanoscale imaging with single nitrogen-vacancy centres. *Nature Nanotech.* **7,** 320–324 (2012).

Author contributions
B.J.M.H., I.B. and V.V. contributed equally to this work. M.L. and I.B. conceived and, together with B.J.M.H. and V.V., designed the experiment. The theoretical studies, numerical modelling and design were carried out by I.B. and V.V. Devices were fabricated by B.J.M.H., V.V. and P.D., who also performed the experiments. Data were analysed by B.J.M.H. and V.V. and discussed by all authors. B.J.M.H., V.V. and M.L. wrote the manuscript in discussion with all authors. M.L. is the principal investigator of the project.

Additional information
Reprints and permissions information is available online at www.nature.com/reprints. Correspondence and requests for materials should be addressed to M.L.

Competing financial interests
The authors declare no competing financial interests.